

Generation of acoustical Bessel-like collimated beams using ring-excited flat plate structure transducers

Ming-Liang Han(韩明亮), Ruo-Yu Tang(唐若昱), Ning Ma(马宁), Guang-Bin Zhang(张光斌), and Xiao-Feng Zhang(张小凤)

Citation: Chin. Phys. B, 2025, 34 (**4**): 040702. DOI: 10.1088/1674-1056/adb38c
Journal homepage: http://cpb.iphy.ac.cn; http://iopscience.iop.org/cpb

What follows is a list of articles you may be interested in

Static-to-kinematic modeling and experimental validation of tendon-driven quasi continuum manipulators with nonconstant subsegment stiffness

Xian-Jie Zheng(郑先杰), Meng Ding(丁萌), Liao-Xue Liu(刘辽雪), Lu Wang(王璐), and Yu Guo(郭毓)
Chin. Phys. B, 2024, 33 (**1**): 010703. DOI: 10.1088/1674-1056/acfaf8

Real-time programmable coding metasurface antenna for multibeam switching and scanning

Jia-Yu Yu(余佳宇), Qiu-Rong Zheng(郑秋容)†, Bin Zhang(张斌), Jie He(贺杰), Xiang-Ming Hu(胡湘明), and Jie Liu(刘杰)
Chin. Phys. B, 2022, 31 (**9**): 090704. DOI: 10.1088/1674-1056/ac80b2

A comparative study on radiation reliability of composite channel InP high electron mobility transistors

Jia-Jia Zhang(张佳佳), Peng Ding(丁芃), Ya-Nan Jin(靳雅楠), Sheng-Hao Meng(孟圣皓), Xiang-Qian Zhao(赵向前), Yan-Fei Hu(胡彦飞), Ying-Hui Zhong(钟英辉), and Zhi Jin(金智)
Chin. Phys. B, 2021, 30 (**7**): 070702. DOI: 10.1088/1674-1056/abe2fd

Magnetic shielding property for cylinder with circular, square, and equilateral triangle holes

Si-Yuan Hao(郝思源), Xiao-Ping Lou(娄小平), Jing Zhu(祝静), Guang-Wei Chen(陈广伟), and Hui-Yu Li(李慧宇)
Chin. Phys. B, 2021, 30 (**6**): 060702. DOI: 10.1088/1674-1056/abeeee

Theoretical analysis and experimental validation of radial cascaded composite ultrasonic transducer

Xiao-Yu Wang(王晓宇), Zhi-Xin Yu(余芷欣), Jing Hu(胡静), and Shu-Yu Lin(林书玉)
Chin. Phys. B, 2021, 30 (**4**): 040701. DOI: 10.1088/1674-1056/abd399

Generation of acoustical Bessel-like collimated beams using ring-excited flat plate structure transducers

Ming-Liang Han(韩明亮)[1], Ruo-Yu Tang(唐若昱)[2], Ning Ma(马宁)[1], Guang-Bin Zhang(张光斌)[1,†], and Xiao-Feng Zhang(张小凤)[1]

[1] *Shaanxi Key Laboratory of Ultrasonics, College of Physics and Information Technology, Shaanxi Normal University, Xi'an* 710119, *China*
[2] *College of Electronic Information and Optical Engineering, Nankai University, Tianjin* 300071, *China*

(Received 2 December 2024; revised manuscript received 21 January 2025; accepted manuscript online 7 February 2025)

This paper proposes a method to generate Bessel-like collimated beams with suppressed side lobes using the flexural vibration modes of a fixed boundary circular plate, which is excited by a longitudinally vibrating transducer in a ring excitation manner. The factors affecting the generation of Bessel-like collimated beams are investigated by theoretical analysis, numerical simulation and experimental methods. The results indicate that Bessel-like wave can be generated by a thin circular plate with fixed boundaries. The third-order mode of the circular plate can be modified to generate a collimated beam with suppressing side lobes when it is excited in a ring excitation manner and the excitation position lies between the first two nodal circles of the plate. As the excitation radius increases, the main lobe width of the resulting Bessel-like collimated beam decreases, the extent of the focusing region increases, and the amplitude of the side lobes initially increases and then decreases. Based on the simulation results, a prototype Bessel-like collimated beam generation system is made and measured experimentally. The experimental results are in good agreement with the numerical results. The Bessel-like collimated beam can be generated by the proposed system, which has potential application in the fields of long-range detection, imaging of highly attenuated materials, and airflow acceleration.

Keywords: Bessel-like collimated beams, flat plate structure transducers, flexural vibration, ring-excited

PACS: 07.07.Mp, 07.05.Tp, 43.40.+s, 07.64.+z

DOI: 10.1088/1674-1056/adb38c **CSTR:** 32038.14.CPB.adb38c

1. Introduction

Bessel beams are employed extensively in the field of acoustics due to their non-diffractive no angular spread and self-healing characteristics.[1–4] There has been a significant interest in the study of an acoustic Bessel beams. For example, a lot of research had carried out on the acoustic radiation force exerted by standing wave tweezers utilizing zero-order or higher order Bessel beams, and these findings have been effectively utilized for particle trapping and manipulation applications.[5–9] Furthermore, benefiting from the characteristic of the highly concentrated central peak and long depth-of-focus,[10–12] Bessel-like beams have a wide range of applications in imaging fields, including medical imaging,[13,14] borehole imaging,[15] and subsurface imaging,[16,17] which can significantly improve image resolution and reduce image spherical aberration.[18] In addition, Bessel-like beams exhibit promise for a number of potential applications, including non-invasive neuronal stimulation,[19] non-destructive testing,[20] and airflow manipulation.[21]

The method to produce Bessel beams can be divided into passive and active ways.[22] The passive approach to generating a Bessel-like beam is to use acoustic lenses to transform existing beams.[23,24] Daniel *et al*. used the Soret zone plate with a pupil mask to generate acoustic quasi-Bessel beams with sub-wavelength transverse dimensions.[25] Tang *et al*. proposed an effective metasurface to construct a two-dimensional (2D) acoustic half-Bessel beam, which is based on an array of spatially varied coiling-slit units and each unit mimics the wave responses derived from the expression of the acoustic half-Bessel beam.[26] While acoustic lenses can be designed to achieve beam focusing and modulation effects through refraction or diffraction, the design process is inherently complex and costly. The active approach is a direct generator of Bessel-like waves, primarily through the utilization of specific transducer configurations or phased arrays. Hsu *et al*. employed non-uniformly polarized piezoelectric discs with full-thickness electric field strengths approximating a Bessel function along the radial direction to generate Bessel-like waves by applying a single voltage excitation to the piezoelectric disc.[27] Campbell *et al*. generated frequency-independent Bessel-like waves using a ring-array PZT with weighted Bessel-like voltage excitation of the individual electrodes.[28] Shi *et al*. designed a device consisting of two omnidirectional equifrequency interdigital transducers to generate a high-intensity, stable, and uniform energy distribution quasi-Bessel surface acoustic wave for microparticle manipulation.[29] Although the aforementioned studies can be employed to generate Bessel-like beams, the generated acous-

†Corresponding author. E-mail: guangbinzhang@snnu.edu.cn

© 2025 Chinese Physical Society and IOP Publishing Ltd. All rights, including for text and data mining, AI training, and similar technologies, are reserved.

tic waves are accompanied by high frequencies and substantial sidelobes. Consequently, it is necessary to suppress the side flaps of the Bessel-like waves to form a collimated beam.

In recent years, a number of methods have been proposed for generating low-frequency Bessel collimated beams,[30–33] which can likewise be divided into passive and active types according to the beam generation method. Hu *et al*. proposed a collimated acoustic lens that can propagate 125 wavelengths in air by combining a zigzag-shaped structure with an array of subwavelength resonators on an ultra-thin planar structure.[34] Tian *et al*. proposed a bilateral symmetric zig–zag structure on the basis of Hu *et al*.'s study, which reduced the longitudinal scale of the material from 1/15 to 1/33 of the wavelength, reducing the size of the material and broadening its application range.[35] Moreover, phononic crystal structure is used to form a collimated acoustic lens.[36] Shen *et al*. generated a collimated beam with a frequency of 0.792 Hz using a 2D phononic crystal structure.[37] Cervenka *et al*. designed an acoustic lens consisting of a gradient refractive index phononic crystal, which consists of a series of toroidal scat terers, to convert acoustic waves generated by a miniaturized ultrasonic transducer into a collimated beam.[38] Daliasa *et al*. designed an acoustic lens by combining conical lens shapes, phononic crystals and asymptotic refractive index design concepts. A plane wave in the frequency range of 4 kHz to 8 kHz can be converted into a Bessel-like collimated beam using these structures.[39] Although all of the above passive methods can produce Bessel-like collimated beams. However, there is a significant loss of acoustic waves after passing through the lens, and in addition the complex structure and large size may limit their application.[40] The active method is to use a single transducer or a transducer array to directly generate a low-frequency Bessel collimated beam.[41] Chillara *et al*. generated low-frequency Bessel beams utilizing the radial vibration mode of a single piezoelectric ceramic plate, which has lower frequency and good collimation characteristics.[42–44] However, the intensity of acoustic waves generated by a single piezoelectric ceramic sheet is limited due to the power capacity and size limitations of the individual piezoelectric ceramics. Additionally, for some applications in air, such as airflow acceleration, aerosol, and ultrasonic defoaming, the radial vibration mode of a single piezoelectric plate also suffers from impedance mismatch issues.

To address the above issues, this paper proposes a Bessel-like acoustic wave generation system based on flexural vibration modes of a thin circular plate with fixed boundary. The factors affecting the generation of Bessel-like collimated beams are investigated by numerical simulation and experimental methods. The collimated beam generated by the proposed system can be used in the fields of long-range detection,[45,46] imaging of highly attenuated materials,[47,48] and airflow acceleration.[21]

2. Methodology

2.1. Theoretical method

Assuming that the radius of a thin plate is R, and its thickness is H. Based on the Kirchhoff–Love hypothesis, the differential equation for a thin plate of uniform thickness under harmonic axisymmetric vibration can be described as[49]

$$\nabla^4 Y(\rho) - k_{\mathrm{p}}^4 Y(\rho) = 0, \tag{1}$$

where $Y(\rho)$ is the transverse vibration displacement, and k_{p} is the wave number of the plate, which is defined as

$$k_{\mathrm{p}} = \omega^2 (\rho_v H/D), \tag{2}$$

in which ρ_v is the density of the plate, $D = EH^3/[12(1-v^2)]$ is the flexural vibration stiffness of the plate, E is the Young's modulus, and v is the Poisson's ratio.

The generalized solution of Eq. (1) can be expressed as follows:[49]

$$\begin{aligned} Y(\rho) = {} & [A\mathrm{J}_0(k_{\mathrm{p}}\rho) + B\mathrm{Y}_0(k_{\mathrm{p}}\rho) \\ & + C\mathrm{I}_0(k_{\mathrm{p}}\rho) + D\mathrm{K}_0(k_{\mathrm{p}}\rho)]\,\mathrm{e}^{\mathrm{j}\omega t}, \end{aligned} \tag{3}$$

where $\mathrm{J}_0(k_{\mathrm{p}}\rho)$, $\mathrm{Y}_0(k_{\mathrm{p}}\rho)$ are the first- and second-type zero-order Bessel functions, and $\mathrm{I}_0(k_{\mathrm{p}}\rho)$, $\mathrm{K}_0(k_{\mathrm{p}}\rho)$ are the first and second type zero-order corrected Bessel functions, respectively. A, B, C, and D are coefficients that can be determined by the boundary conditions.

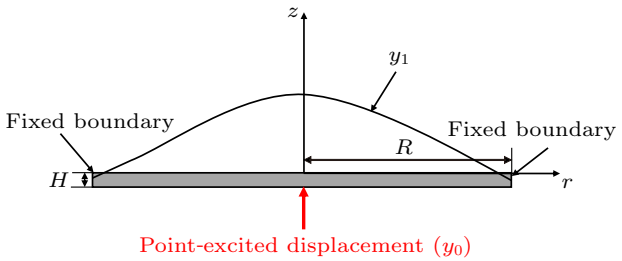


Fig. 1. Schematic diagram of the structure of the PFP.

Figure 1 shows the schematic diagram of the structure of a point-excited circular plate (PFP). Here, y_0 is the excitation displacement, and y_1 is the transverse vibration displacement of the PFP. To illustrate its vibration mode, figure 1 shows the first-order transverse vibration displacement of the PFP. Since the values of both $\mathrm{Y}_0(k_{\mathrm{p}}\rho)$ and $\mathrm{K}_0(k_{\mathrm{p}}\rho)$ are infinite when $\rho = 0$, while in reality the displacement of the center of the circular plate cannot be infinite, the coefficients B an D must be zero. Therefore, for the PFP, equation (3) can be rewritten as

$$y_1 = [A_1\mathrm{J}_0(k_{\mathrm{p}}\rho) + C_1\mathrm{I}_0(k_{\mathrm{p}}\rho)]\,\mathrm{e}^{\mathrm{j}\omega t}, \tag{4}$$

where $\rho \in [0, R]$. Considering that the boundary of the circular plate is fixed, the boundary condition can be expressed as

$$y_1(R) = 0, \quad y_1'(R) = 0. \tag{5}$$

Considering the point excitation, at the excitation position, the displacement conditions can be written as

$$y_1(0) = y_0. \tag{6}$$

Combining Eqs. (4)–(6), the coefficients A_1 and C_1 can be determined. The normal vibration velocity of a PFP can be expressed as

$$u_1 = -\mathrm{j}\omega[A_1 \mathrm{J}_0(k_\mathrm{p}\rho) + C_1 \mathrm{I}_0(k_\mathrm{p}\rho)]. \tag{7}$$

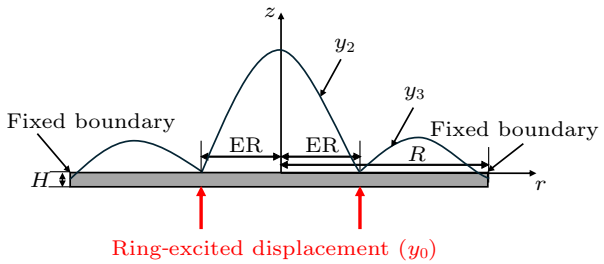


Fig. 2. Schematic diagram of the structure of the RFP.

Figure 2 shows the schematic of the structure of the ring-excited circular plate (PFP), it can be divided into two regions, the outside excitation circle ring and the inside excitation circle. y_2 and y_3 are the normal vibration displacements of the inner and outer ring parts, respectively. The normal vibration displacement of an RFP can be expressed as

$$y_2 = [A_2 \mathrm{J}_0(k_\mathrm{p}\rho) + C_2 \mathrm{I}_0(k_\mathrm{p}\rho)]\mathrm{e}^{\mathrm{j}\omega t}, \tag{8}$$

in which $\rho \in [0, ER]$, ER is the ring excitation radius.

$$\begin{aligned} y_3 = {} & [A_3 \mathrm{J}_0(k_\mathrm{p}\rho) + B_3 \mathrm{Y}_0(k_\mathrm{p}\rho) \\ & + C_3 \mathrm{I}_0(k_\mathrm{p}\rho) + D_3 \mathrm{K}_0(k_\mathrm{p}\rho)]\mathrm{e}^{\mathrm{j}\omega t}, \end{aligned} \tag{9}$$

in which $\rho \in [ER, R]$, considering that the boundary of the circular plate is fixed, the boundary condition can be expressed as

$$y_3(R) = 0, \quad y_3'(R) = 0. \tag{10}$$

At the excitation position, the continuity conditions can be written as

$$y_2(ER) = y_3(ER) = y_0, \tag{11}$$

$$Q(y_2)_{\rho=ER} = Q(y_3)_{\rho=ER} = F_0, \tag{12}$$

where F_0 is the transverse shear constant at the excitation position, and $Q(Y)_\rho$ is the transverse shear force with the expression

$$Q(Y)_\rho = -D\left(\frac{\partial^3 Y}{\partial \rho^3} + \frac{1}{\rho}\frac{\partial^2 Y}{\partial \rho^2} - \frac{1}{\rho^2}\frac{\partial Y}{\partial \rho}\right). \tag{13}$$

Combining Eqs. (8)–(13), the coefficients A_2, C_2, A_3, B_3, C_3, and D_3 of Eqs. (8) and (9) can be determined. Subsequently, the normal vibration velocity of an RFP can be expressed as

$$u_2 = -\mathrm{j}\omega[A_2 \mathrm{J}_0(k_\mathrm{p}\rho) + C_2 \mathrm{I}_0(k_\mathrm{p}\rho)]\mathrm{e}^{\mathrm{j}\omega t}, \tag{14}$$

$$\begin{aligned} u_3 = {} & -\mathrm{j}\omega[A_3 \mathrm{J}_0(k_\mathrm{p}\rho) + B_3 \mathrm{Y}_0(k_\mathrm{p}\rho) \\ & + C_3 \mathrm{I}_0(k_\mathrm{p}\rho) + D_3 \mathrm{K}_0(k_\mathrm{p}\rho)]\mathrm{e}^{\mathrm{j}\omega t}. \end{aligned} \tag{15}$$

For both PFP and RFP, the plate vibrates in its axisymmetric modes of all orders, which can be regarded as harmonic vibrations with angular frequency ω. Vibration propagates along the z-axis, the characteristic radius of the sound source is R. Based on the Khokhlov–Zabolotskaya–Kuznetsov (KZK) equations, the solution of the finite-beam ultrasonic radiation acoustic field under a quasilinear approximation can be expressed as follows:[50–52]

$$\begin{aligned} \bar{p}(\sigma, \xi) = {} & \rho_0 c_0 \int_0^\infty \frac{2\mathrm{j}}{\sigma} u(\xi') \\ & \times \exp\left(-\mathrm{j}\frac{\xi^2 + \xi'^2}{\sigma}\right) \mathrm{J}_0\left(\frac{2\xi\xi'}{\sigma}\right) \xi' \mathrm{d}\xi', \end{aligned} \tag{16}$$

where $\sigma = z/r_0$ and $\xi = \rho/R$ are the axial and radial dimensionless coordinates, respectively. R and r_0 are the reference coordinates, R is chosen to be the radius of the sound source, $r_0 = kR^2/2$ is called the Rayleigh distance, and k is the wave number. ρ_0 and c_0 are the density of the medium and the speed of sound, respectively. ξ' denotes the radial coordinate at the surface of the sound source. $u(\xi')$ denotes the transverse vibration velocity distribution at the surface of sound source. According to Eqs. (7), (14)–(16), the distribution of the sound field can be determined.

2.2. Simulation method

Figure 3 shows the schematic structure of the transducer excited circular plate radiation system and its simplified finite element model. The proposed system consists of three parts: the driver, the amplifier, and the radiator. The driver is a Langevin-type longitudinal vibration transducer, which can generate longitudinal vibrations when an applied voltage is exerted. The amplifier is a stepped ultrasonic horn that serves amplification and frequency matching. The radiator is a fixed-boundary thin circular plate that exhibits flexural vibration under longitudinal excitation and radiates a Bessel-like beam into the surrounding medium.

For the vibrating system shown in Fig. 3, a stepped ultrasonic horn and a stepped circular tube ultrasonic horn are applied to serve as amplifiers to excite a thin circular plate with a fixed boundary under point excitation and ring excitation, which can be thought as a point-excited circular plate (PFP) and a ring-excited circular plate (RFP), respectively. In order to explore the factors affecting the generation of Bessel-like collimated beams, a simplified model of the system was built in the numerical analysis software COMSOL Multiphysics 6.1. The excitation area is shown in Fig. 3 as a blue circle. In finite element simulation, the plate is excited by adding a displacement of 10 nm along the positive Z-axis at the bottom

of the circular plate. A thin circular metal plate with a radius of $R = 52$ mm, a thickness of $H = 5$ mm, and a material comprising 7075 aluminum alloy was used in our study. The density of the 7075 aluminum was 2650 kg/m^3, the Young's modulus was 7×10^{10} N/m^2, and the Poisson's ratio was 0.33. A semi-circular air domain with a perfect match layer is added above the plate, which has the density of 1.29 kg/m^3 and the speed of sound of 340 m/s. An infinity hard boundary is chosen at the bottom of the air domain to simulate the unidirectional radiation of a thin circular plate embedded in an infinity baffle. The mesh size of the circular plate is set to one-sixth of the wavelength of the plate's flexural vibration at the highest frequency. The mesh size of the sound domain is set to one-sixth of the wavelength of the air at the highest frequency. The PML domain was swept with eight distributions along the thickness direction.

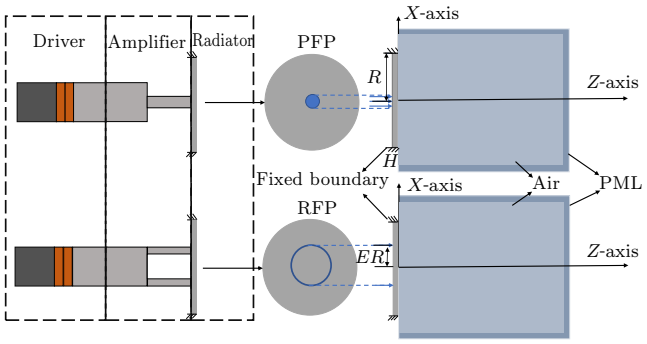


Fig. 3. Schematic diagram of the structure of the Bessel-like acoustic wave generation system and its finite element model.

2.3. Experiment

In order to verify the simulation results, we design and manufacture an RFP excited by an ultrasonics transducer to radiate Bessel acoustic beam in air, as shown in Fig. 4. A 1045 steel ring is installed at the top surfaces of the circular plate to realize the fixed boundary. The density of the 1045 steel was 7850 kg/m^3, the Young's modulus was 20.5×10^{10} N/m^2, and the Poisson's ratio was 0.28. Twenty M5 bolt holes are drilled evenly around the circumference of the steel ring, and the plate can be clamped between the upper and lower steel rings with bolts. The plate steel ring is fixed to the steel tube on its lower side. The materials used for the steel ring and steel tube are the same as those utilized for the mass block subsequent to the transducer.

For the Langevin-type transducer, the materials of the thicknesses of the back mass block, piezoelectric ceramic, and front mass block are 1045 steel, PZT-8, and 7075 aluminum alloy, with thicknesses of are L_1, $2L_2$, and L_3, respectively, and the radius of all three is R_2. The density of the PZT-8 was 8700 kg/m^3, and the Young's modulus was 11×10^{10} N/m^2. For the ultrasonic horn, the material is 7075 aluminum alloy, the thickness of the solid cylinder and the hollow round tube are identical, and the total length is L_4, the inner radius of the circular tube is R_1, and the outer radius is R_2. For the thin circular plate, the material is 7075 aluminum alloy, the thickness is H and the effective radius is R. The dimensions parameters of each part are shown in Table 1.

Table 1. The dimensional parameters of the system.

Size	L_1	L_2	L_3	L_4	R_1	R_2	R	H
Value (mm)	45	6.5	25	122	20	25	52	5

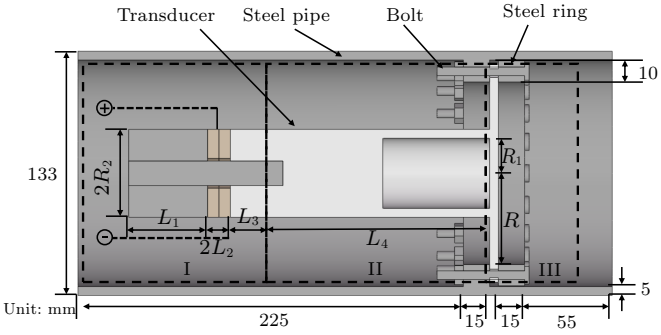


Fig. 4. Schematic diagram of the structure of a Bessel-like acoustic wave generation system.

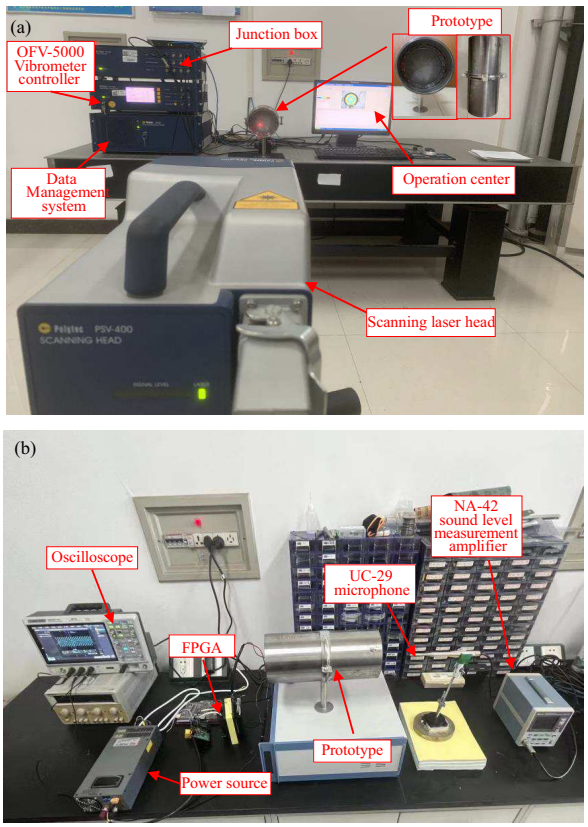


Fig. 5. Diagram of the equipment used for the experiment: (a) face-scanning laser vibrometer, (b) sound level measurement amplifier.

A prototype Bessel-like collimated beam generation system is made and measured experimentally with the experimental equipment shown in Fig. 5. The vibration distribution on the surface of the circular plate was tested with a Polytech OFV-5000 Doppler laser vibrometer (Polytech GMbH, Baden-Württemberg, Germany). The transducer was excited by a si-

nusoidal signal with a frequency of 31.039 kHz and a peak-to-peak value of 5 V. The axial sound pressure distribution of the system at $x = 0$ and the radial sound pressure distribution of the system at $z = 0.3$ m were tested using an acoustic pressure probe (a 1/4-inch (1 inch = 2.54 cm) diameter UC-29 microphone).

3. Results and discussion

Figure 6(a) illustrates the simulation results of the initial four orders flexural vibration modes of the PFP. The corresponding frequencies are 4.60 kHz, 16.97 kHz, 35.39 kHz, and 57.98 kHz, respectively. Figure 6(b) illustrates the numerical results of the radiated sound field in these modes. The results demonstrate that the flexural vibration of PFP can indeed be effectively employed to generate Bessel-like waves. However, the Bessel-like beam produced by PFP exhibits a large number of side lobes. Moreover, with the vibrational order, the number of side lobes increases.

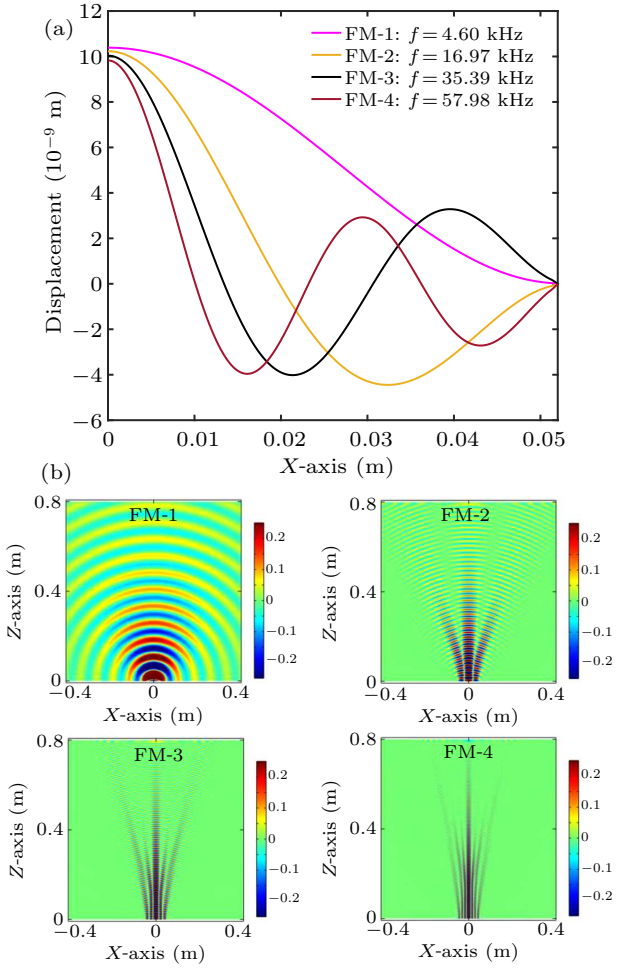


Fig. 6. The vibration modes and normalized sound field distribution of the first four orders of the flexural vibration of a PFP: (a) vibration modes, (b) sound field distribution.

Figure 7 presents the normalized normal displacement and its Bessel fitting results of the FM-3 vibration mode. These results are obtained using both the finite element method (FEM) and the theoretical computation (Eq. (7)). From Fig. 7, it can be seen that the theoretical and FEM results are basically in agreement, and the normal displacement distribution of the PFP is similar to that of $J_0(\alpha r)$ ($\alpha = 169.0$ m^{-1}). Combining Eqs. (6), (7), and (16), it can be concluded that the PFP can generate Bessel-like beams which can be verified from the simulation results.

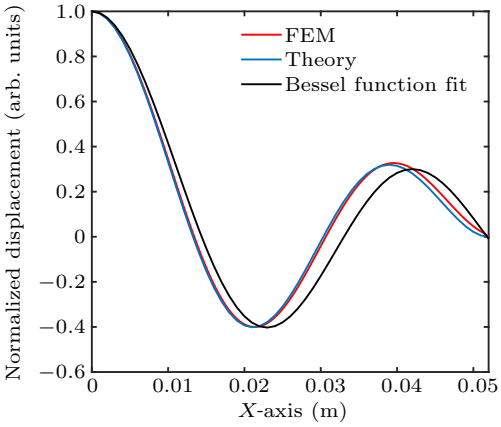


Fig. 7. The normalized normal displacement in the FM-3 vibration mode and its corresponding Bessel function fit ($J_0(\alpha r), \alpha = 169.0$ m^{-1}).

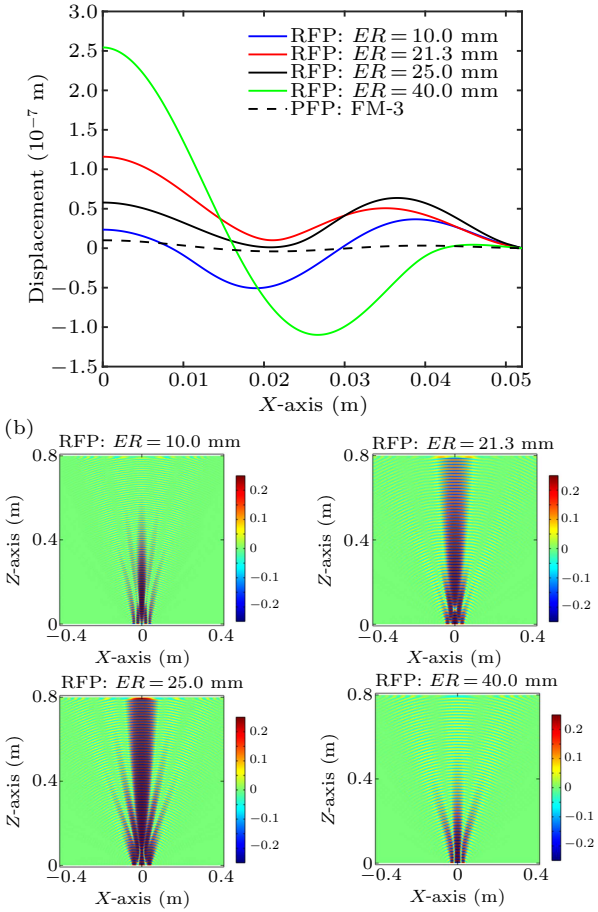


Fig. 8. The vibration modes and normalized sound field distribution of an RFP under different excitation regions: (a) vibration modes, (b) sound field distribution.

Generally, the FM-3 vibration mode of a circular plate can be divided into three excitation regions by three nodal circles.

Due to the fact that the vibration displacements between adjacent nodes are in opposite directions, then phase cancellation occurs, which results in large sidelobes. Thus, the sidelobes of generated Bessel-like wave can be suppressed by reducing the inverse region of the normal vibrational displacement. So, in this paper, we propose a method to generate a side-lobes suppressed collimation Bessel-like wave with a ring-excited fixed boundary flexural vibration thin circular plate. The vibration characteristics and its radiation sound field under different excitation regions are simulated by adding ring excitations in different excitation regions. The numerical results are presented in Fig. 8.

From Fig. 8(a), it can be observed that the vibration modes of an RFP are different from those of a PFP. With the excitation displacement of 10 nm, the vibration displacement of an RFP exhibits a significantly higher amplitude than that of a PFP. And they also exhibit notable discrepancies across different excitation radius (ER). To further investigate the effect of the excitation conditions on the vibration displacements of the system, the average normal vibration displacements (ANVD) of PFP and RFP were extracted under a displacement excitation of 10 nm, respectively, and the results are presented in Tables 2 and 3. As illustrated in Table 2, the number of nodal circles in the PFP increases with the increase of vibration order. The ANVDs of PFP exhibit a decreased tendency due to the opposite vibration directions on both sides of the nodal circles. All the values are less than 10 nm.

Table 2. The ANVD of the PFP under 10-nm displacement excitation.

Mode	PFP: FM-1	PFP: FM-2	PFP: FM-3	PFP: FM-4
ANVD (nm)	5.37	0.82	1.62	0.55

Table 3. The ANVD of the RFP under 10-nm displacement excitation.

Mode	RFP: $ER = 10.0$ mm	RFP: $ER = 21.3$ mm	RFP: $ER = 25.0$ mm	RFP: $ER = 40.0$ mm
ANVD (nm)	0.89	44.53	33.19	22.37

Next, we discuss the effect of the excitation region on the distribution of the radiated sound field of the RFP, as shown in Figs. 8(a) and 8(b). When excitation radius (ER) is 10 mm, the corresponding excitation region is situated within the nodal circular 1 (excitation region 1). In this mode, the number of nodal circles of the RFP is identical to that of the FM-3 of the PFP. However, in contrast to the FM-3 of PFP, RFP exhibits a smaller relative displacement at its center. The displacement of the RFP is significantly greater than that of the PFP. However, the proportion of the displacement reversal region of RFP is increased, resulting in a lower ANVD of the RFP relative to FM-3 mode of PFP. From Fig. 8(b), we can find that the number of the side lobes remains consistent for both modes. But the magnitude of the side lobes is more pronounced for the RFP. Consequently, the introduction of a ring excitation within the nodal circular 1 of the thin circular plate with a fixed boundary results in an augmentation of the side lobes.

When ER is 21.3 mm and 25 mm, the excitation region is situated between nodal circular 1 and nodal circular 2 (excitation region 2). In both modes, there is only one nodal circular for each RFP, and the vibration direction on the surface of the circular plate is consistent. The ANVD of the RFP are 44.53 nm and 33.19 nm, which are 27.48 and 20.48 times higher than the ANVD of FM-3 for PFP. As a result, both the displacement and the acoustic radiation directivity of the circular plate have been significantly enhanced. As illustrated in Fig. 8(b), the number of side lobes, as well as the sidelobe amplitude of the Bessel-like wave generated by an RFP, is markedly reduced when the collimation of the central beam is maintained. However, compared to $ER = 25$ mm, the sidelobes were better suppressed when ER was 21.3 mm. The normalized normal vibrational displacements of the RFP for both excitation radii, as well as their Bessel-fit curves ($|\mathrm{J}_0(\alpha r)|\,(\alpha = 106.3\ \mathrm{m}^{-1})$), were calculated, as illustrated in Fig. 9. In can be observed that a general agreement exists between the theoretical and FEM results. When $ER = 21.3$ mm, the normalized normal displacement of the RFP exhibits greater overlap with the Bessel fitting results ($|\mathrm{J}_0(\alpha r)|\,(\alpha = 106.3\ \mathrm{m}^{-1})$), thereby facilitating enhanced suppression of the sidelobes.

When ER is 40 mm, the excitation region is situated between nodal circular 2 and nodal circular 3 (excitation region 3). Given that the vibration displacement of the RFP between the excitation position is nearly zero, the number of nodal circulars of the RFP is approximately two and its vibration mode is like that of the PFP's FM-2. However, the displacement at the center of the RFP is substantially increased in this mode under identical excitation. The ANVD of the RFP is 22.37 nm, which is 20.48 times the ANVD for a PFP at FM-2 mode. In combination with Fig. 6(b), it can be observed that the shapes of the Bessel-like beams formed by the RFP and PFP are also essentially identical, exhibiting two side lobes in both cases. However, combining Fig. 6(a) as well as Fig. 8(a), it can be seen that for the same displacement (10 nm) excitation, the displacements of the PFP at FM-2 mode as well as the RFP at $ER = 40$ mm at the center of the circular plate are 10 nm, 257 nm, respectively. The magnitude of the vibrational displacement of the source is proportional to the intensity of its radiated sound waves. It can conclude that the addition of

ring excitation to excitation region 3 of the thin circular plate with fixed boundary results in a reduction in the number of side lobes and an improvement of the acoustic radiation of the plate.

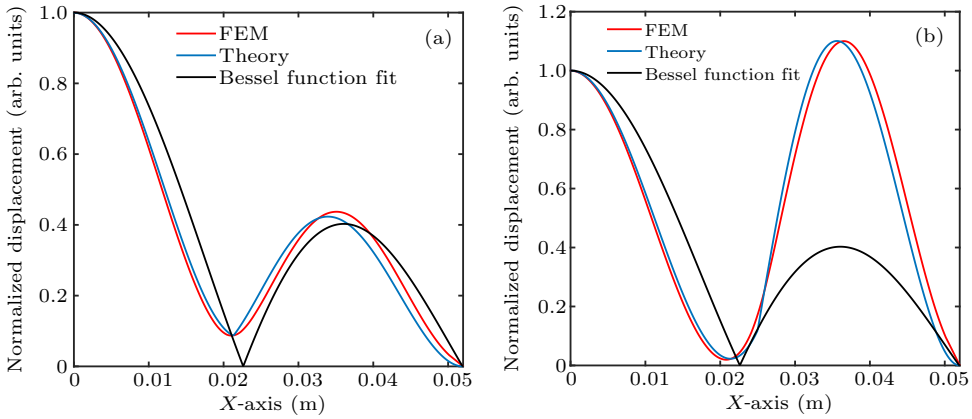


Fig. 9. The normalized normal displacement of the RFP and its corresponding Bessel function fit ($|\mathrm{J}_0(\alpha r)|$ ($\alpha = 106.3$ m^{-1})): (a) $ER =$ 21.3 mm, (b) $ER = 25$ mm.

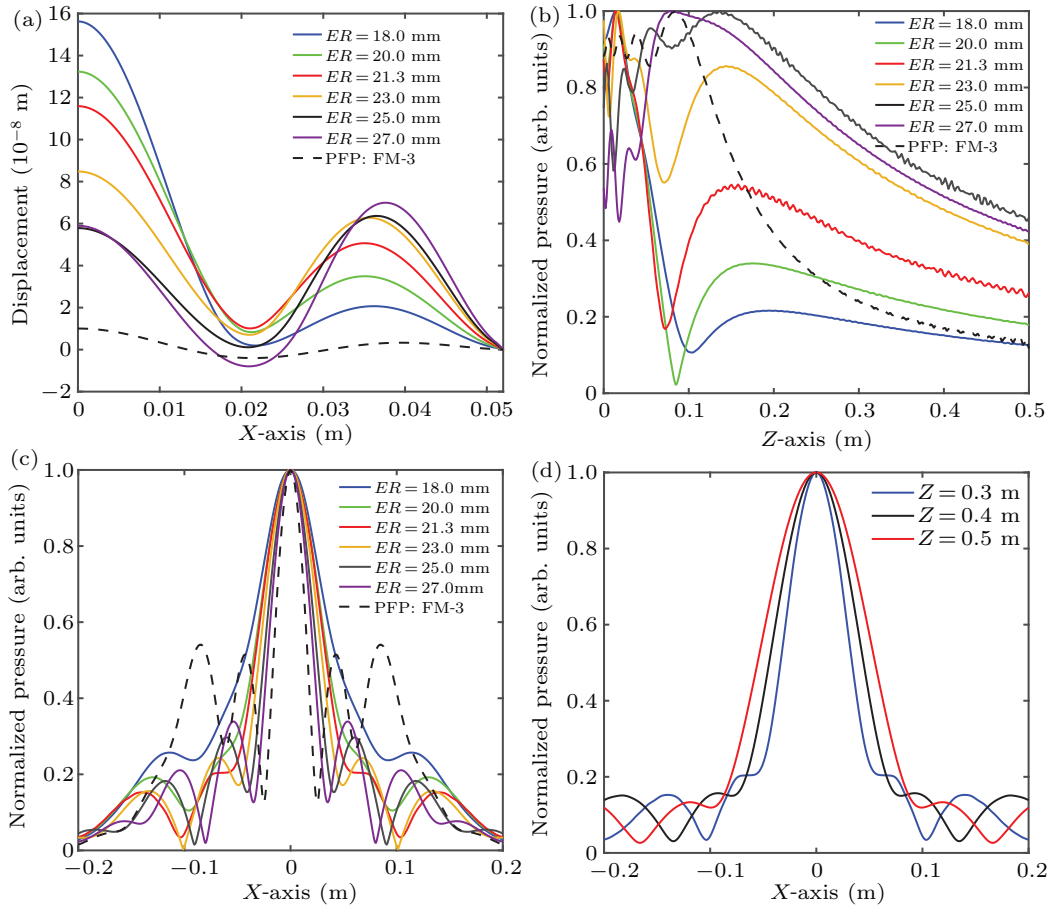


Fig. 10. The vibration modes of an RFP and the normalized sound field distributions at different excitation radius: (a) vibration modes, (b) Z-axis sound pressure distribution at $X = 0$, (c) radial sound pressure distribution at $Z = 0.3$ m with different ER, (d) radial sound pressure distribution when $ER = 21.3$ mm.

Then the vibration modes and radiation sound field distribution of the RFP at different ER in the excitation region 2 are simulated and the results are shown in Fig. 10. From Fig. 10(a), we can see that the displacement at the center of the circular plate decreases, while the displacement near the boundary increases with the increase of ER. The ANVD extracted at different ERs reveals that the ANVD of an RFP initially rises and then declines with the increase of ER. The maximum value of ANVD is attained at $ER = 21.3$ mm, with the excitation position situated within the valley of the displacement curve of RFP. Combining Figs. 10(b) and 10(c), when the plate is excited at the excitation region 2 in a circular manner, both Bessel-like beams generated by the RPF have smaller side lobes as well as a more extensive focus region than those

of a PFP with the same-size. The attenuation of their sound waves along the axial direction is greatly reduced, which is in line with the characteristics of collimated beams. The vibration distribution on the surface of the circular plate has an influence on the depth of focused region, the width of the main lobe, and the width of the side lobes. The depth of the focused region increases with the excitation radius (ER). However, it is noteworthy that although the peak on the right side is the highest at $ER = 27$ mm, the number of nodal circulars changes from one to three under this excitation condition, and the phase cancellation occurs. Consequently, the maximum value of the focus depth appeared at $ER = 25$ mm. The width of the main lobe decreases with the increase of the excitation radius. However, the amplitude of the side lobes achieves the minimum at $ER = 21.3$ mm, which is because the vibration distribution on the surface of the circular plate under this excitation condition is closer to the zeroth-order Bessel function ($|\mathrm{J}_0(\alpha r)|\,(\alpha = 106.3\ \mathrm{m}^{-1})$). Finally, from Fig. 10(d), the generated beam maintains good collimation as well as low side lobes at different axial distances.

The experimental results are shown in Fig. 11, in which the analytical results are also presented for a comparison. Table 4 shows the FEM and experimental results are presented for the sidelobe-amplitude, as well as the beam-width and focusdepth at full width at half maximum (FWHM). It can be seen from Fig. 11(a) that the vibration directions of the radiator surfaces are basically the same with the negative values only appeared in the excited area. The reason is that the working frequency of the system is slightly higher than the optimal vibration frequency of the circular plate. In future designs, the frequency of the longitudinal excitation source will be adjusted to make the radiator work at its resonance frequency. From Figs. 11(b), 11(c), and Table 3, we can observe that the generated Bessel-like beam has a narrow main lobe width and small side lobe amplitude, with the axial sound pressure first decreasing and then increasing, showing a secondary focusing effect. The experimental results are in general agreement with the characteristics of collimated Bessel beams. Nevertheless, the experimental results indicated a little pronounced side-lobe amplitude. The main factor contributing to this discrepancy is that an infinity baffle was not installed in the experiment, which means that radiation from the back of the transducer may affect the sound field in front of the transducer.

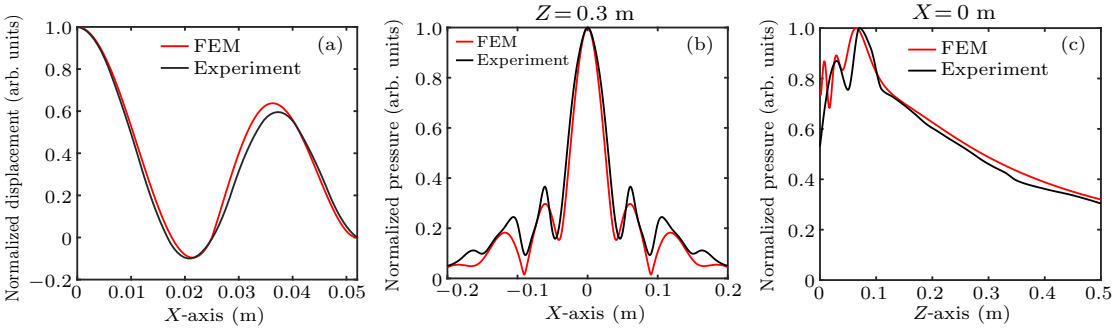


Fig. 11. Comparisons of simulation and experimental results: (a) schematic diagram of the prototype, vibration modes; (b) $Z = 0.3$ m, radial sound pressure distribution; (c) $X = 0$ m, axial sound pressure distribution.

Table 4. Comparisons of simulation and experimental results: sidelobe-amplitude, as well as the beam-width and focusdepth at full width at half maximum (FWHM).

	Sidelobe-amplitude	Beam-width (mm)	Focusdepth (mm)
Analytical	0.31	50.1	290.0
Experimental	0.38	60.0	206.5

4. Conclusion

To conclude, we have proposed a method based on theoretical analysis to generate Bessel-like collimated beams with suppressed side lobes using the flexural vibration modes of a fixed boundary metal plate under ring excitation. The factors affecting the generation of Bessel-like collimated beams are investigated numerically. The results indicate that Bessel-like waves can be generated by a thin circular plate with fixed boundaries when the excitation type is pointing excitation. The third-order mode of the circular plate can be modified to generate a collimated beam with suppressing side lobes when it is excited in a ring, which is situated between the first two nodal circles of the plate. As the excitation radius increases, the main lobe width of the resulting Bessel-like collimated beam decreases, the extent of the focusing region increases, and the amplitude of the side lobes initially increases and then decreases. A prototype Bessel-like collimated beam generation system is made and measured experimentally. A longitudinally vibrating transducer is used to excite the plate, which has a low radiation impedance and high radiation efficiency, thereby can weaken the power capacity limitations of existing methods. The experimental results are in good agreement with the numerical results. The collimated beam generated by the proposed system can be used in the fields of long-range detection, imaging of highly attenuated materials, and airflow acceleration.

Acknowledgement

Project supported by the National Natural Science Foundation of China (Grant No. 12474440).

References

[1] Durnin J 1987 *J. Opt. Soc. Am. A* **4** 651
[2] Durnin J, Miceli J J Jr and Eberly J H 1987 *Phys. Rev. Lett.* **58** 1499
[3] Antonacci G, Caprini D and Ruocco G 2019 *Appl. Phys. Lett.* **114** 013502
[4] Qiao X L, Cheng X M, Zhang Q, Zhang W D, Ren Z Y and Bai J T 2023 *Chin. Phys. B* **32** 048703
[5] Jiménez N, Picó R, Sánchez-Morcillo V, Romero-García V, García-Raffi L M and Staliunas 2016 *Phys. Rev. E* **94** 053004
[6] Mitri F G and Fellah Z E A 2008 *IEEE Trans. Ultrason. Ferroelectr. Freq. Control.* **55** 2469
[7] Chen B, Wu Y, Ao Z, Cai H, Nunez A, Liu Y, Foley J, Nephew K, Lu X and Guo F 2019 *Lab. Chip.* **19** 1755
[8] Wang A T, Yu L H, Li J F and Liang X Y 2023 *Chin. Phys. B* **32** 044201
[9] Li S Y, Shi J Y, Zhang X F and Zhang G B 2019 *J. Acoust. Soc. Am.* **145** 3233
[10] McGloin D and Dholakia K 2005 *Contemp Phys.* **46** 15
[11] Vetter C, Steinkopf R, Bergner K, Ornigotti M, Nolte S, Gross H and Szameit A 2019 *Laser Photon. Rev.* **13** 1900103
[12] Ji J Y, Zheng Z G, Zhu J L, Wang L, Wang X G and Zhao S M 2024 *Chin. Phys. B* **33** 014204
[13] Lu J Y and Greenleaf J F 1990 *IEEE Trans. Ultrason. Ferroelectr. Freq. Control* **37** 438
[14] Lu J Y and Greenleaf J F 1992 *IEEE Trans. Ultrason. Ferroelectr. Freq. Control* **39** 19
[15] Chen Y, Gao K, Davis E S, Sinha D N, Pantea C and Huang L 2018 *Appl. Phys. Lett.* **113** 071903
[16] Vu C K, Sinha D N, Pantea C, Nihei K T, Schmitt D P and Skelt C (U.S. patent) 8 259 530 [2012-09- 4]
[17] Vu C K, Sinha D N, Pantea C, Nihei K T, Schmitt D P and Skelt C (U.S. patent) 8 559 269 [2013-10-15]
[18] Chillara V K, Pantea C and Sinha D N 2018 *Wave Motion* **76** 19
[19] Köhrmann K U, Michel M S, Steidler A, Marlinghaus E, Kraut O and Alken P 2002 *BJU Int.* **90** 248
[20] Lu J Y and Greenleaf J F 1993 *Ultrason. Imaging* **15** 134
[21] Hasegawa K, Qiu L W, Noda A, Inoue S and Shinoda H 2017 *Appl. Phys. Lett.* **111** 064104
[22] Turunen J, Vasara A and Friberg A T 1988 *Appl. Opt.* **27** 3959
[23] Zhao Y, Dong H Y, Zhao S W, Min S, Cheng J, Li B, Chi F F and Liu S 2019 *J. Appl. Phys.* **126** 065103
[24] Bai L, Dong H Y, Song G Y, Cheng Q, Huang B, Jiang W X and Cui T J 2018 *Adv. Mater. Technol.* **3** 1800064
[25] Tarrazó-Serrano D, Castiñeira-Ibáñez S, Minin O V, Candelas P, Rubio C and Minin I V 2019 *Sensors* **19** 378
[26] Ye L, Qiu C, Lu J, Tang K, Jia H, Ke M, Peng S and Liu Z 2016 *AIP Adv.* **6** 085007
[27] Hsu D, Margetan F and Thompson D 1989 *Appl. Phys. Lett.* **55** 2066
[28] Campbell J A and Soloway S 1990 *J. Acoust. Soc. Am.* **88** 2467
[29] Shi J, Zhang C, Li P, Peng B, Li X, Liu X and Zhou W 2024 *Appl. Phys. Lett.* **124** 202201
[30] Alvarez-Arenas T E G, Camacho J and Fritsch C 2016 *Ultrasonics* **67** 85
[31] Alanazi A M, Venkatakrishnan S, Santos-Villalobos H, Buzzard G T and Bouman C 2023 *IEEE Trans. Comput. Imaging* **9** 904
[32] Jiménez-Gambín S, Jiménez N, Benlloch J M and Camarena F 2019 *Sci. Rep.* **9** 21104
[33] Candelas P, Pérez-López S and Fuster J M 2021 *Sensors* **21** 6086
[34] Hu J, Liang B and Qiu X J 2019 *Appl. Phys. Express* **12** 027002
[35] Tian R, Zhao H and Hu J 2024 *Appl. Phys. Express* **17** 014003
[36] Vanel A L, Dubois M, Tronche C, Fu S, Wang Y T, Dupont G, Rakic A D, Bertling K, Abdeddaim R, Enoch S, Craster R, Li G, Guenneau S and Perchoux J 2024 *New J. Phys.* **26** 073021
[37] Shen F F, Zhu H W, Zhu G, Shi Q F and Schulte J 2020 *Chin. J. Phys.* **63** 201
[38] Cervenka M and Bednarík M 2021 *J. Acoust. Soc. Am.* **149** 4534
[39] Dasila S, Krishnamurthy C V and Subramanian V 2024 *J. Appl. Phys.* **135** 024903
[40] Deng J, Guasch O and Zheng L 2021 *Int. J. Mech. Sci.* **194** 106179
[41] Wang C H, Qi B Y, Lin M Y, Zhang Z R, Makihata M, Liu B Y, Zhou S, Huang Y H, Hu H J, Gu Y, Chen S, Lei Y S, Lee, T, Chien S, Jang K I, Kistler E B and Xu S 2021 *Nat. Biomed. Eng.* **5** 749
[42] Chillara V K, Pantea C and Sinha D N 2017 *Appl. Phys. Lett.* **110** 064101
[43] Chillara V K, Davis E S, Pantea C and Sinha D N 2019 *Ultrasonics* **96** 140
[44] Greenhall J, Chillara V K, Sinha D N and Pantea C 2021 *J. Vib. Acoust.* **143** 064501
[45] Gamarra-Diezma J L, Miranda-Fuentes A, Llorens J, Cuenca A, Blanco-Roldán G L and Rodríguez-Lizana A 2015 *Sensors* **15** 2902
[46] Asakura Y, Okubo K and Tagawa N 2017 *Jpn. J. Appl. Phys.* **56** 07JC14
[47] Hutchins D A, Watson R L, Davis L A J, Akanji L, Billson D R, Burrascano P, Laureti S and Ricci M. 2020 *Sensors* **20** 2285
[48] Govind B, Jiang X Y, Bart S and Hartwell P 2022 *Sens. J.* **22** 145
[49] Han M L, Zhang G B and Zhang X F 2024 *Ultrasonics* **144** 107441
[50] Ding D S 2000 *Phys. Rev. E* **61** 2038
[51] Dai Y R and Ding D S 2011 *Acta Phys. Sin.* **60** 124302 (in Chinese)
[52] Ding D S and Huang J H 2016 *Chin. Phys. B* **25** 124307